

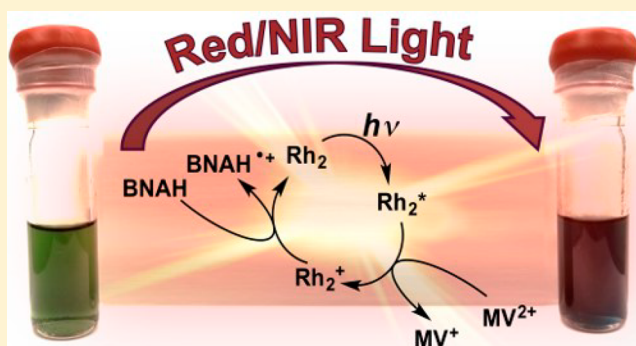
New Rh₂(II,II) Complexes for Solar Energy Applications: Panchromatic Absorption and Excited-State Reactivity

Tyler J. Whittimore, Hannah J. Sayre, Congcong Xue, Travis A. White,[†] Judith C. Gallucci, and Claudia Turro^{*†}

Department of Chemistry and Biochemistry, The Ohio State University, Columbus, Ohio 43210, United States

S Supporting Information

ABSTRACT: The new heteroleptic paddlewheel complexes *cis*-[Rh₂(μ -form)₂(μ -np)] [BF₄]₂, where form = *p*-ditolylformamidinate (DTolF) or *p*-difluorobenzylformamidinate (F-form) and np = 1,8-naphthyridine, and *cis*-Rh₂(μ -form)₂(μ -npCOO)₂ (npCOO⁻ = 1,8-naphthyridine-2-carboxylate), were synthesized and characterized. The complexes absorb strongly throughout the ultraviolet ($\lambda_{\text{max}} = 300 \text{ nm}$, $\epsilon = 20\,300 \text{ M}^{-1} \text{ cm}^{-1}$) and visible regions ($\lambda_{\text{max}} = 640 \text{ nm}$, $\epsilon = 3500 \text{ M}^{-1} \text{ cm}^{-1}$), making them potentially useful new dyes with panchromatic light absorption for solar energy conversion applications. Ultrafast and nanosecond transient absorption and time-resolved infrared spectroscopies were used to characterize the identity and dynamics of the excited states, where singlet and triplet Rh₂/form-to-naphthyridine, metal/ligand-to-ligand charge-transfer (ML-LCT) excited states were observed in all four complexes. The npCOO⁻ complexes exhibit red-shifted absorption profiles extending into the near-IR and undergo photoinitiated electron transfer to generate reduced methyl viologen, a species that persists in the presence of a sacrificial donor. The energy of the triplet excited state of each complex was estimated from energy-transfer quenching experiments using a series of organic triplet donors ($E(^3\pi\pi^*)$ from 1.83 to 0.78 eV). The singlet reduction (+0.6 V vs Ag/AgCl) potentials, and singlet and triplet oxidation potentials (−1.1 and −0.5 V vs Ag/AgCl, respectively) were determined. Based on the excited-state lifetimes and redox properties, these complexes represent a new class of light absorbers with potential application as dyes for charge injection into semiconductor solar cells and in sensitizer-catalyst assemblies for photocatalysis that operate with irradiation from the ultraviolet to ~800 nm.



INTRODUCTION

Worldwide energy use has been increasing since the dawn of the Industrial Revolution in the early 1800s and, according to the 2016 Key World Energy Statistics, the total world energy consumption was the equivalent of 9425 million tons of oil in 2014, which can be converted to 12.4 TW.¹ Sunlight has the potential to satisfy the global energy demands since it has been estimated that more energy strikes the earth's surface in 1.5 h than humans use in a year.² One challenge in harvesting the solar output is that not every photon is usable because many are scattered and the frequency of others is too low to drive useful reactions.^{3,4} But a large portion of the remaining incident light in the visible and near-infrared (near-IR) spectral regions are not absorbed by traditional photosensitizers, such that they remain unused in light harvesting and dye-sensitized applications. In fact, the extension of the dye absorption profile to utilize the solar photon flux in the red and near-infrared spectral regions was recently identified as a challenge in the field and is vital to increasing the productivity of these systems.^{5,6}

In order to improve the conversion of solar energy, new molecules with excited states capable of photoredox reactions

are needed with strong panchromatic absorption profiles from the ultraviolet to the near-IR ranges.^{6,7} The development of new light absorbers is critical in the fields of dye-sensitized solar,^{6–8} photocatalytic,^{9,10} and photoelectrosynthetic cells.⁵ Each of these methods has traditionally utilized a photosensitizer that is anchored to a p- or n-type semiconductor and undergoes hole or electron injection, respectively, upon photoexcitation, thus producing current or driving useful chemical reactions.

Ruthenium(II) polypyridyl complexes, such as the thiocyanate-based N3 dye, have dominated dye-sensitized solar cell (DSSC) research since their discovery owing to their robustness, high extinction coefficients, and sufficiently long-lived excited states ($\geq 20 \text{ ns}$).^{8,11,12} However, these dyes suffer from nonradiative deactivation through thiocyanate ligands and limited absorption at wavelengths $>600 \text{ nm}$.^{6,8,11} Efforts using squaraine,^{13,14} porphyrins,^{15–17} phthalocyanines,¹⁸ and other dyes have recently been undertaken for n-type sensitization in the red and near-IR spectral regions. There are fewer dyes

Received: August 10, 2017

Published: October 4, 2017

currently available for hole injection into p-type semiconductors; the N3 dye does not generate photocurrent, but there has recently been promise with “push-pull” organic dyes and triphenylamine-containing systems coupled to a strong light absorber.^{19,20}

Several properties of bimetallic complexes make them good candidates to function as photosensitizers, including light absorption throughout the visible and near-IR spectral ranges, directional ligand/metal-to-ligand charge-transfer (ML-LCT) states for electron and hole transfer, ability to store holes and electrons in the ligands and various oxidation states available to the bimetallic core, and large tunability of excited-state and redox properties through ligand substitution.^{21–23} Dirhodium(II,II) complexes are of particular interest owing to their facile synthesis, robustness in water and oxygen-rich environments, and the recently reported large absorption cross sections displayed by formamidinate-bridged architectures.^{22,24} The present work focuses on the investigation of the excited-state and redox properties of the series of complexes depicted in Figure 1, *cis*-[Rh₂(μ-DTolF)₂(μ-np)₂][BF₄]₂ (**1**; DTolF = *p*-

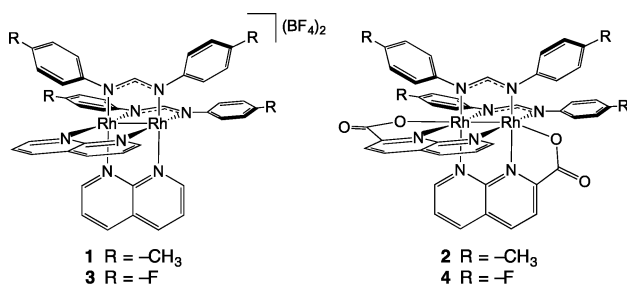


Figure 1. Molecular structures of 1–4.

ditolylformamidinate, np = 1,8-naphthyridine), *cis*-Rh₂(μ-DTolF)₂(μ-npCOO)₂ (**2**; npCOO[−] = 1,8-naphthyridine-2-carboxylate), *cis*-[Rh₂(μ-F-Form)₂(μ-np)₂][BF₄]₂ (**3**; F-form = *p*-difluorobenzylformamidinate), and *cis*-Rh₂(μ-F-Form)₂(μ-npCOO)₂ (**4**). Complexes 1–4 possess broad light absorption from the ultraviolet into the near-IR range and favorable excited-state and redox properties, making them potentially useful for dye-sensitized solar cell and photocatalysis applications.

EXPERIMENTAL SECTION

Materials. All reactions were performed under inert atmosphere. Syntheses involving np and npCOO were protected from light by covering reactions and manipulations when possible with aluminum foil. Sample preparations involving a sacrificial electron donor were performed in the dark. Solvents and reagents were used as received unless otherwise stated. Filtration and manipulation of synthesized complexes were performed in open air unless specifically stated. The 1,8-naphthyridine and 1,8 naphthyridine-2-carboxylic acid ligands were purchased from TCI and Life Chemicals, respectively. Acetonitrile, acetone, dimethylformamide, diethyl ether, and chloroform were purchased from Fisher Scientific and dimethyl sulfoxide was procured from Sigma-Aldrich in a sealed bottle. All other reagents were purchased from Sigma-Aldrich. A Barnstead B-Pure system was used to deionize water (18 MΩ) and acetonitrile was distilled over calcium hydride prior to use. Dimethyl sulfoxide-*d*₆ (DMSO-*d*₆) for ¹H NMR and time-resolved IR (TRIR) experiments was purchased in ampules from Sigma-Aldrich. Methyl viologen (MV²⁺) dichloride was obtained from Sigma-Aldrich, and the hexafluorophosphate salt was recovered by metathesis using excess NH₄PF₆ in deionized H₂O. The complexes [Rh₂(DTolF)₂(CH₃CN)₆][BF₄]₂, [Rh₂(F-Form)₂(CH₃CN)₆][BF₄]₂,²⁵ and [Rh₂(DTolF)₂(np)₂][BF₄]₂ were synthesized using

previously reported procedures.²⁴ Complex **3** was prepared in a similar manner as **1**, but using [Rh₂(F-Form)₂(ACN)₆][BF₄]₂ as the starting material.

cis-Rh₂(DTolF)₂(npCOO)₂ (**2**). A solution of 15 mL distilled CH₃CN containing *cis*-[Rh₂(DTolF)₂(CH₃CN)₆][BF₄]₂ (66 mg, 0.060 mmol) and 1,8-naphthyridine-2-carboxylic acid (25 mg, 0.14 mmol) was heated at reflux for 3 h. The reaction mixture was filtered while hot and water (70 mL) was added to the blue solution. Crystals formed at −4 °C within 24 h and were rinsed with ~50 mL water then 25 mL ether. Yield = 36 mg, (58%). ¹H NMR (DMSO-*d*₆, 400 MHz, 298 K) δ/ppm: 9.82 (2H, *d*, μ-npCOO), 8.61 (2H, *d*, μ-npCOO), 8.45 (2H, *d*, μ-npCOO), 7.95 (2H, *d*, μ-npCOO), 7.92 (2H, *dd*, μ-npCOO), 7.44 (4H, *d*, phenyl), 7.24 (2H, *t*, NCHN), 7.11 (4H, *d*, phenyl), 6.60 (4H, *t*, NCHN), 5.97 (4H, *d*, phenyl), 2.30 (6H, *s*, -CH₃), 2.07 (6H, *s*, -CH₃). ESI-MS(+): [M + 2H]²⁺ *m/z* = 500.0 (calc. *m/z* = 500.0); [M + H]⁺ *m/z* = 999.1 (calc. *m/z* = 999.1).

cis-[Rh₂(F-Form)₂(np)₂][BF₄]₂ (**3**). A 20 mL solution of distilled CH₃CN containing *cis*-[Rh₂(F-Form)₂(CH₃CN)₆][BF₄]₂ (50 mg, 0.044 mmol) and 1,8-naphthyridine (20 mg, 0.15 mmol) in was heated at reflux for 3 h. The reaction mixture was filtered while hot and the solvent was removed under rotary evaporation. The purple product was dissolved in minimal CH₃OH and precipitated with ether. Yield = 33 mg, (67%). ¹H NMR (DMSO-*d*₆, 400 MHz, 298 K) δ/ppm: 9.41 (4H, *s*, μ-np), 8.81 (4H, *d*, μ-np), 7.95 (4H, *m*, μ-np), 7.60 (2H, *t*, NCHN), 7.05 (8H, *dd*, phenyl), 6.67 (8H, *dd*, phenyl). ESI-MS(+): [M]²⁺ *m/z* = 464.0 (calc. *m/z* = 464.0).

cis-Rh₂(F-Form)₂(npCOO)₂ (**4**). In a manner similar to the synthesis of **2**, a solution consisting of *cis*-[Rh₂(F-Form)₂(CH₃CN)₆][BF₄]₂ (50 mg, 0.044 mmol) and 1,8-naphthyridine-2-carboxylic acid (28 mg, 0.16 mmol) in 20 mL distilled CH₃CN was heated at reflux for 3 h. The reaction mixture was filtered while hot. Water (70 mL) was added to the blue solution. Crystals formed at −4 °C within 24 h and were rinsed with ~50 mL water then 25 mL ether. Yield = 23 mg, (43%). ¹H NMR (DMSO-*d*₆, 400 MHz, 298 K) δ/ppm: 9.85 (2H, *d*, μ-npCOO), 8.64 (2H, *d*, μ-npCOO), 8.45 (2H, *d*, μ-npCOO), 8.00 (2H, *d*, μ-npCOO), 7.94 (2H, *dd*, μ-npCOO), 7.60 (4H, *dd*, phenyl), 7.34 (2H, *t*, NCHN), 7.15 (4H, *t*, phenyl), 6.65 (4H, *t*, phenyl), 6.10 (4H, *dd*, phenyl). ESI-MS(+): [M]⁺ *m/z* = 1014.0 (calc. *m/z* = 1014.0).

Instrumentation and Methods. ¹H NMR spectra were measured in DMSO-*d*₆ using a Bruker DPX 400 MHz spectrometer at 298 K. Chemical shifts (δ) given in ppm were referenced to the residual DMSO-*d*₆ solvent signal at 2.50 ppm.²⁶ Electropray ionization mass spectra, (+)ESI-MS, were recorded in positive mode using a Bruker MicroTOF mass spectrometer by dissolving the sample in CH₃CN prior to injection. Solid phase IR spectra were obtained using a Thermo Fisher Nicolet iS10 FT-IR spectrometer equipped with a mid-infrared IR source, a XT-KBr beamsplitter, and a DTGS-KBr detector. The attenuated total reflectance (ATR) accessory used was a Smart iTRTM accessory equipped with a diamond window and spectra were the result of 16 to 32 scans. Electronic absorption spectra were collected using an Agilent 8453 diode array spectrophotometer with 1 nm resolution at 298 K using 1 cm path length quartz cuvettes. Molar extinction coefficients were determined from triplicate stock solutions consisting of a 1–2 mg sample (Mettler Toledo XSE105 DualRange) in DMSO and measured by dilution in triplicate.

Cyclic voltammetry experiments were carried out under an inert atmosphere using a BASi CV-50W potentiostat. A three-electrode cell was used with a glassy carbon disc (3 mm) working electrode, Pt wire auxiliary electrode and Ag/AgCl (NaCl) reference electrode. A 0.1 M ⁿBu₄NPF₆/CH₃CN electrolyte solution was used with an applied scan rate of 200 mV/s. Experimental details for spectroelectrochemistry experiments are provided in the Supporting Information (SI).

Crystals of **2** suitable for X-ray diffraction were grown via slow evaporation in DMSO. The data collection was undertaken using a dark brown rectangular crystal. Examination of the diffraction pattern on a Nonius Kappa Apex II CCD diffractometer indicated a monoclinic crystal system. All work was conducted at 150 K using an Oxford Cryosystems Cryostream Cooler. The data collection strategy was set up to measure a quadrant of reciprocal space with a redundancy target of 6. Phi and omega scans with a frame width of

0.5° were used. The data were collected using the program APEX2 and processed using the program SAINT within APEX2.^{27,28} The data were scaled, and absorption and beam corrections were made based on the multi-scan technique as implemented in SADABS.²⁹ The structure was solved by the direct methods procedure in SHELXT. Full-matrix least-squares refinements based on F^2 were performed in SHELXL-2014/7,³⁰ as incorporated in the WinGX package.³⁰ The asymmetric unit consists of the Rh dimer, two solvent molecules of DMSO and one molecule of water. There are intermolecular hydrogen bonds between these solvent molecules. For the methyl groups, the hydrogen atoms were added at calculated positions using a riding model with $U(H) = 1.5U_{eq}$ (bonded carbon atom). The torsion angle, which defines the orientation of the methyl group about the C–C or S–C bonds, was refined. The rest of the hydrogen atoms were included in the model at calculated positions using a riding model with $U(H) = 1.2U_{eq}$ (bonded atom). The hydrogen atoms of the water molecule were refined isotropically. The final refinement cycle was based on 11789 intensities and 656 variables and resulted in agreement factors of $R1(F) = 0.042$ and $wR2(F^2) = 0.089$. For the subset of data with $I > 2\sigma(I)$, the $R1(F)$ value is 0.032 for 9481 reflections. The final difference electron density map contains maximum and minimum peak heights of 1.72 and $-0.56 \text{ e}/\text{\AA}^3$. Neutral atom scattering factors were used and include terms for anomalous dispersion.³¹

Transient absorption spectroscopy with nanosecond/microsecond time resolution (nsTA) was performed on a home-built system that has been previously described in detail.³² The frequency doubled output of a 10 Hz Nd:YAG source (532 nm, fwhm ~ 8 ns, ~ 5 mJ/pulse) was used to excite the deoxygenated samples with 0.5–0.8 OD at the excitation wavelength in a 1 cm path length quartz cuvette. Femtosecond transient absorption (fsTA) experiments were performed on an instrument previously described in detail.³³ The samples were excited with 2.5 to 3.5 $\mu\text{J}/\text{pulse}$ at the sample using the frequency-doubled output of the optical parametric amplifier (OPA) signal (Coherent, OPerA Solo). The instrument response function (IRF) was determined to be 85 fs via the Kerr optical effect in cyclohexane. A 1 mm path length Harrick Scientific flow cell was equipped with 1 mm CaF_2 windows and a ~ 5 mL sample volume flowed for the duration of the experiment. The polarization angle between the pump and probe pulses was set to the magic angle to avoid the effects of rotational diffusion. The measurements were all averaged for multiple retroreflector cycles and all spectra were corrected for chirp in the white light continuum. Kinetic traces were plotted and analyzed using the sum of exponential terms with Igor Pro (6.3) software. All fits differed in multiple cycles by $<5\%$ and the error of each exponential fit was generally found to be between 4 and 7%.

The instrument used to conduct ultrafast time-resolved infrared spectroscopy (TRIR) has been reported previously with modifications outlined in the SI.³⁴ TRIR was performed with a Ti:sapphire regenerative amplifier (Coherent, Legend; 1 kHz; fwhm = 300 fs) seeded by a short pulse oscillator (Coherent, Mantis, fwhm = < 20 fs). The complexes were excited into the red side of their lowest absorption bands using $\lambda_{\text{exc}} = 600$ nm light for **1** and **3** and $\lambda_{\text{exc}} = 700$ nm **2** and **4** (2 $\mu\text{J}/\text{pulse}$) with frequency doubled output of the signal from an optical parametric amplifier (Coherent, OPerA), which was then filtered using dichroic mirrors and focused onto an optical delay line.

The triplet energies, E_{00}^T , of **1–4** were estimated through the quenching of the lifetimes of the long-lived triplet excited states of a series of organic sensitizers monitored by transient absorption spectroscopy. In these experiments, Stern–Volmer plots, τ_0/τ vs $[\text{Rh}_2 \text{ complex}]$, were constructed using anthracene ($E^T = 1.83 \text{ eV}$, $\tau_0 = 46.5 \mu\text{s}$), perylene ($E^T = 1.53 \text{ eV}$, $\tau_0 = 17.4 \mu\text{s}$), rubrene ($E^T = 1.15$, $\tau_0 = 39.5 \mu\text{s}$), and β -carotene ($E^T = 0.78$, $\tau_0 = 19 \mu\text{s}$) as the energy-transfer donors and **1–4** as the Rh_2 quenchers in DMSO.³⁵ Except for rubrene, which was excited at 532 nm (5 mJ/pulse), all other organic sensitizers were excited at 355 nm (5 mJ/pulse). Bimolecular electron transfer from 300 μM solutions of **2** or **4** to MV^{2+} dichloride was determined by the addition of 100-fold excess the acceptor in 1:5 $\text{H}_2\text{O}:\text{CH}_3\text{CN}$ or the PF_6^- salt in DMSO; solutions were prepared such that the complex had an absorbance of 0.5 OD at the excitation

wavelength, 532 nm. Steady-state photoinitiated electron transfer was investigated using a solution of 300 μM of **2**, 0.05 M 1-benzyl-1,4-dihydronicotinamide (BNAH) as a sacrificial electron donor, and 2 mM MV^{2+} in 1:1 $\text{CH}_3\text{CN}/\text{H}_2\text{O}$ irradiated with a 150 W Xe arc lamp (USHIO) using a 610 nm long-pass filter. Low temperature absorption measurements were performed in a specially built Dewar equipped with a 1 cm quartz cell.

Molecular and electronic structure calculations were performed with standard density functional theory (DFT) methods using the Gaussian 09 package on the singlet states of **1–4** using the Ohio Supercomputer Center.³⁶ A 6-31g* basis set was used for all non-Rh atoms and the Stuttgart–Dresden (SDD) energy-consistent pseudopotential was used for Rh.³⁷ For **1** and **3**, which are expected to bind solvent in the axial positions, two acetonitrile ligands were coordinated to the axial sites to provide a more realistic solution structure and to allow for comparison to previous calculations.²⁴ The substitution of axial CH_3CN ligands for O-bound DMSO in **1** resulted in Rh–Rh bond lengths and HOMO–LUMO gaps that differed by less than 1%. Analysis of the Gaussian 09 outputs were carried out in GaussView 5.0.36.³⁸ Full optimization was performed using crystal structures of related complexes as starting points, and a polarizable continuum model was utilized to mimic the solvation effects of DMSO. Frequency and force constant analyses were carried out to confirm that the proposed structures were the global minima. The final structure of **2** was consistent with the crystallographic data for the complex. Molecular orbital compositions and analyses, as well as Mayer bond orders were completed using the AOMix program.³⁹

RESULTS AND DISCUSSION

X-ray Crystal Structure. The molecular structure of **2** was determined using X-ray crystallography and consists of a dirhodium core bridged by two DTolF[−] ligands and two npCOO^- ligands (Figure 2). The latter are coordinated

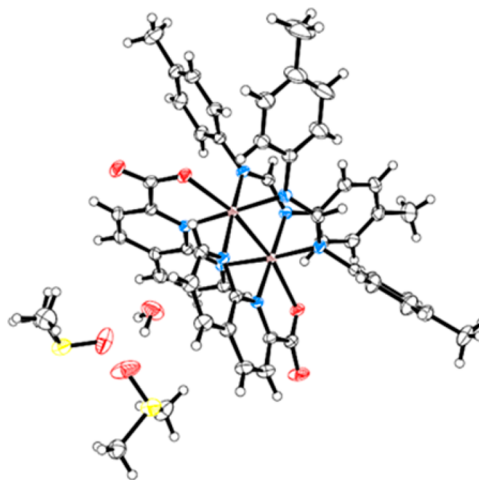


Figure 2. Crystal structure of **2** (ellipsoids drawn at 50% probability).

equatorially through the two N atoms on the np portion of the ligand and axially through one of the carboxylate oxygen atoms, as depicted in Figure 2 and shown schematically in Figure 1. Both rhodium axial sites are bound by the carboxylate group of each npCOO^- ligand with Rh–O bond lengths of 2.251(2) and 2.247(2) Å. The Rh–Rh bond length was determined to be 2.4482(4) Å, which is similar to that reported for $\text{Rh}_2(\text{DTolF})_4$, 2.434 Å,⁴⁰ but is slightly elongated when compared with $\text{Rh}_2(\text{OAc})_2(\text{pynp})_2[\text{BF}_4]_2$ ($\text{pynp} = \eta^3$ -pyridyl-1,8-naphthyridine; $\text{OAc}^- = \text{CH}_3\text{COO}^-$), 2.408 Å.⁴¹ Shorter Rh–Rh bond lengths are typically observed in acetate as compared with formamidinate complexes.⁴⁰ The ability of the

npCOO⁻ ligand to donate electron density at the axial positions may also contribute to elongate the Rh–Rh bond in **2**, a property that is limited in the neutral pynp bridging ligand.

It should be noted that the Rh–Rh bond length in **2** is shorter than in the related series of bis-DTolF *cis*-Rh₂(II,II) partial paddlewheel complexes of the type *cis*-[Rh₂(DTolF)₂(L)₂]²⁺, where L represents a nonbridging, chelating bidentate ligand. For example, Rh–Rh distances of 2.597(1) and 2.5991(9) were determined for *cis*-[Rh₂(DTolF)₂(dppz)₂]²⁺ and for *cis*-[Rh₂(F-Form)₂(dpq)₂]²⁺, respectively.²² The effect of the differences in metal–metal bond lengths on the electronic structure and excited states of these complexes will be discussed in the sections to follow.

Electronic Absorption and Electrochemistry. The steady-state electronic absorption spectra of **1–4** recorded in DMSO are shown in Figures 3 and S1, and pertinent

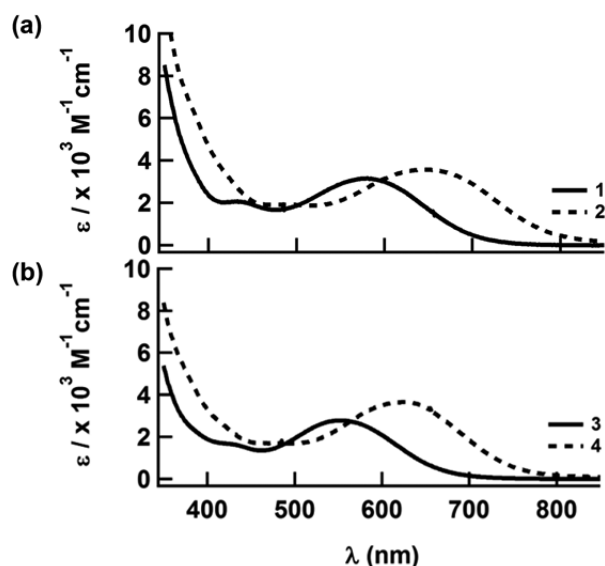


Figure 3. Electronic absorption spectra of (a) **1** and **2** and (b) **3** and **4** in DMSO.

information is listed in Table 1. The absorption spectrum of **3** is similar to that of **1**.²⁴ Complex **1** exhibits ligand-centered $\pi\pi^*$ transitions at 268 ($\epsilon = 31\,200\text{ M}^{-1}\text{ cm}^{-1}$) and 299 nm ($\epsilon = 21\,800\text{ M}^{-1}\text{ cm}^{-1}$), which are consistent with those observed for the free np ligand in MeOH with peaks at 257 nm, 295, 302, and 307 nm.⁴² A low-energy, broad absorption with a maximum at 577 nm ($\epsilon = 3100\text{ M}^{-1}\text{ cm}^{-1}$) is also observed for **1**, previously assigned as a Rh₂($d\pi^*$)/DTolF \rightarrow np(π^*) ML-LCT transition.²⁴ The spectral profile of **3** is similar to that of **1**, but the ML-LCT transition is slightly blue-shifted to 553 nm ($\epsilon = 2800\text{ M}^{-1}\text{ cm}^{-1}$). The shift is attributed to the more

electron-withdrawing character of the F-Form ligand as compared to DTolF, thus removing electron density from the dirhodium core.²²

The electronic absorption spectrum of **2** in DMSO displays $\pi\pi^*$ transitions consistent with those of the free npCOO⁻ ligand, as well as a broad ML-LCT transition with maximum at 640 nm. The red shift of the latter relative to **1** is attributed to increased electron density on the bimetallic core upon axial anion coordination from the npCOO⁻ ligand, making it easier to oxidize, thus lowering the energy of the ML-LCT transition. Compound **4** has a similar electronic absorption spectrum when compared to that of **2**, but with a slightly blue-shifted ML-LCT maximum, 623 nm. This shift is attributed to the lower electron donating character of the F-Form ligand to the bimetallic core when compared to DTolF.

The results from cyclic voltammetry measurements are listed in Table 1 and shown in Figure S2, which indicate that **1** and **2** exhibit reversible Rh₂^{II,III/II,II} couples at +0.87 V and +0.61 V vs Ag/AgCl, respectively. The less positive Rh₂^{II,III/II,II} couple observed for **2** as compared to **1** is attributed to the increased electron density at the rhodium metal center upon carboxylate anion coordination in the former, consistent with the red-shift of the ML-LCT transition of **2** relative to **1**. The first cathodic couples for **1** and **2** are assigned as the reversible one-electron reduction of the np and npCOO⁻ ligands in **1** and **2**, at -0.94 V and -1.07 V vs Ag/AgCl, respectively. The second cathodic couples are assigned as the one-electron reduction of the second np-containing ligand in each complex, observed at $E_{pc} = -1.12\text{ V}$ vs Ag/AgCl in **1** and at $E_{1/2} = -1.28\text{ V}$ vs Ag/AgCl in **2**. The second np-based reduction of **1** results in adsorption to the electrode, a feature that is not observed in **2**. This difference in behavior may be attributed to the blocked axial sites in **2**, precluding its interaction with the electrode. The shift in the Rh₂^{II,III/II,II} electrode potentials between **1** and **2**, 260 mV, is greater than that measured between the first reduction between np and npCOO⁻, 130 mV, which offers evidence that the bathochromic shift in the ML-LCT absorption of **2** is primarily an effect of the increased electron density of the Rh₂ core.

The cyclic voltammograms of **3** and **4** follow similar trends to those of **1** and **2**. The primary difference being that the complexes bridged by F-form ligands, **3** and **4**, are more difficult to oxidize than the corresponding DTolF analogs. In **3** the Rh₂^{II,III/II,II} couple is observed at +1.02 V vs Ag/AgCl, which is 150 mV more positive than that of **1**. In **4**, the $E_{1/2}(\text{Rh}_2^{\text{II,III/II,II}}) = +0.69\text{ V}$ lies at 80 mV more positive than the same couple in **2**. The stabilization of the HOMO in **3** and **4** is attributed to the electron-withdrawing nature of the *p*-F-phenyl substituents in F-Form as compared to the electron donating *p*-Me-phenyl groups in DTolF, as previously reported elsewhere.²² In general, the electrochemistry is consistent with the observed spectral shifts of the ML-LCT transitions in **1–4**.

Table 1. Electronic Absorption Maxima with Molar Absorptivities in DMSO, Reduction Potentials, and Singlet and Triplet Lifetimes for **1–4**

complex	$\lambda_{\text{abs}}/\text{nm}$ ($\epsilon/10^3\text{ M}^{-1}\text{ cm}^{-1}$)	$E_{1/2}/\text{V}$ ($\Delta E_p/\text{mV}$) ^a	τ_s/ps ^c	τ_T/ns ^c
1	268 (31.2), 299 (21.8), 440 (2.0), 577 (3.1)	+0.87 (90), -0.94 (80), -1.12 ^b	13	0.45
2	266 (32.6), 300 (20.3), 490 (1.7), 640 (3.5)	+0.61 (60), -1.07 (70), -1.28 (70)	7	25
3	265 (30.8), 295 (21.9), 428 (1.7), 553 (2.8)	+1.02 (70), -0.88 (80), -1.07 ^b	9	0.58
4	265 (30.3), 296 (19.6), 480 (1.7), 623 (3.6)	+0.69 (80), -1.08 (70), -1.28 (80)	9	25

^aVs Ag/AgCl in 0.1 M Bu₄NPF₆/CH₃CN. ^b E_{pc} value. ^cFrom fsTA in DMSO.

Computational Studies. Electronic structure calculations were performed using Density Functional Theory (DFT) to better understand the photophysical and redox properties of 1–4, and the resulting MO diagrams are shown in Figure 4 and

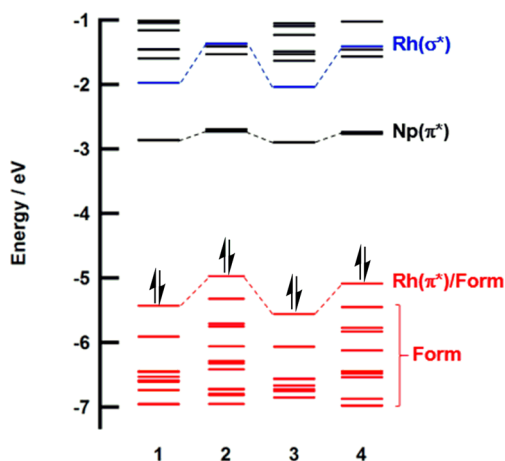


Figure 4. Calculated MO diagrams of 1–4.

electron density maps are depicted in Figure S3. The σ^* - and π^* -metal based orbitals of 2 are calculated to lie at higher energies than the same MOs in 1, attributed to the greater electron density between the two rhodium atoms afforded by the axially coordinated carboxylate anion, an effect also reported in other dirhodium paddlewheel complexes.^{32,40,43–45}

The fact that the $\text{Rh}_2(\pi^*)/\text{DTolF}$ HOMO is destabilized in 2 relative to 1, is consistent with the observation that 2 is easier to oxidize than 1 (Table 1). The np -based LUMO of 2 is slightly destabilized relative to that of 1, also consistent with the electrochemical data (Table 1). Complexes 3 and 4 follow the same trends as 1 and 2, with small shifts associated with the less electron-donating F-Form bridging ligand relative to DTolF. These effects include slightly lower energy calculated $\text{Rh}_2(\pi^*)/\text{F-form}$ HOMO in 3 as compared to the $\text{Rh}_2(\pi^*)/\text{DTolF}$ HOMO in 1, making the former slightly more difficult to oxidize, as observed experimentally (Table 1).

The electron densities of the HOMOs of 1–4 are calculated to possess mixed $\text{Rh}_2(d\pi^*)/\text{formamidinate}$ character, while the electronic contributions of the LUMO and LUMO+1 are localized on a naphthyridine π^* molecular orbitals of np in 1 and 3 and npCOO^- in 2 and 4. The increase in the energy of the occupied Rh_2 MOs with $d\pi^*$ and $d\sigma^*$ character in 2 and 4 relative to 1 and 3, respectively, is consistent with an increase in covalent bonding between the two rhodium centers. To determine the relative changes in Rh-Rh covalency, Mayer bond order calculations were performed, which provide a measure of the covalency vs ionicity of bonds and have been shown to afford useful information in transition metal systems.^{46,47} While there are no significant differences between the calculated Rh-Rh bond distances, the calculated Mayer bond order increases from 0.57 in 1 and 3 to 0.78 in 2 and 4. These results are indicative of greater covalent character between the two metals in the axially coordinated npCOO^- complexes, 2 and 4, as compared to 1 and 3.

Time-Resolved Infrared Spectroscopy. The ground-state IR spectrum of 1 exhibits two asymmetric $\nu(\text{N}=\text{C}-\text{N})$ DTolF stretches at 1507 and 1577 cm^{-1} , and a weaker absorption band at 1608 cm^{-1} , labeled $\nu(\text{form})$ in Table S1 (Figure 5a). The weak peak at 1364 cm^{-1} is attributed to

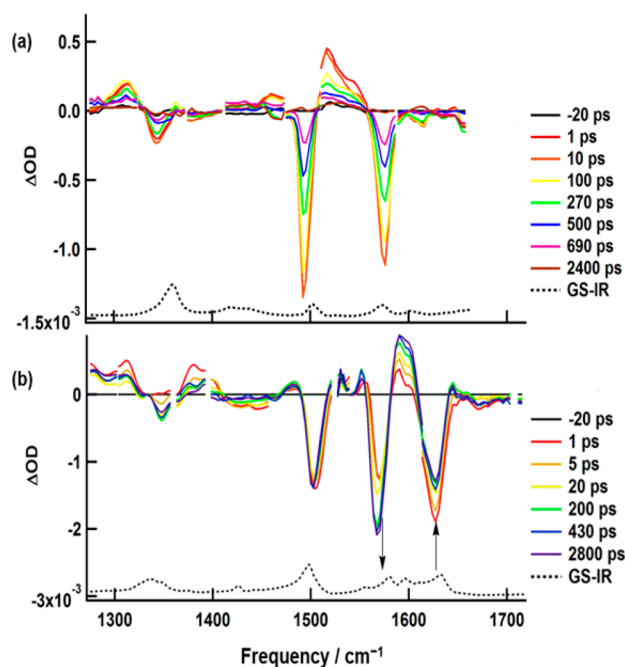


Figure 5. TRIR spectra of (a) 1 ($\lambda_{\text{ex}} = 600 \text{ nm}$, $2 \mu\text{J}$) and (b) 2 ($\lambda_{\text{ex}} = 700 \text{ nm}$, $2 \mu\text{J}$) in $\text{DMSO-}d_6$, along with the corresponding ground-state IR spectra (dashed lines).

phenyl ring stretches of the DTolF ligand, $\nu(\text{Ph-form})$. Peaks at similar positions are also observed in the IR spectra of related $\text{Rh}_2(\text{II,II})$ complexes bridged by DTolF ligands (Figure S4).⁴⁰ The excitation of 1 with a 600 nm pulse (IRF $\approx 170 \text{ fs}$, $2 \mu\text{J}$) results in negative ground-state bleach features at 1343, 1492, 1576 cm^{-1} , and 1608 cm^{-1} (weak), all of which recover with a lifetime of $\sim 420 \text{ ps}$ (Figure S5).

Concomitant with the appearance of ground state bleach features are positive excited-state absorption signals at 1312 cm^{-1} assigned as arising from $\nu(\text{Ph-form})$, and two $\nu(\text{form})$ peaks at 1462 and 1516 cm^{-1} . The signal at 1516 cm^{-1} decays biexponentially with lifetimes of 16 and 424 ps. The shift of these bands to lower energies relative to the corresponding ground-state peaks indicate the loss of electron density from the formamidinate ligand in the excited state, consistent with a $\text{Rh}_2(d\pi^*)/\text{DTolF} \rightarrow \text{np}(\pi^*)$ ML-LCT excited state. The positions of these excited-state peaks are similar at short and long times indicating similar electron density, such that the 16 and 424 ps components are assigned as arising from the lifetimes of the $^1\text{ML-LCT}$ and $^3\text{ML-LCT}$ excited states of 1, respectively. This assignment is supported by the kinetics of the bleach signals at 1492 cm^{-1} and 1576 cm^{-1} , which lack the 16 ps time constant.

While sub-picosecond intersystem crossing (isc) rates are relatively common in transition metal complexes,^{48,49} some bimetallic complexes behave in a manner that parallels traditional organic molecules, including dirhodium(I,I) pyrazolyl, diplatinum(II,II) pyrophosphito, dirhodium(I,I) isocyanide, and a number of quadruply bonded ditungsten and dimolybdenum carboxylates.^{50–53} These bimetallic complexes exhibit relatively long singlet lifetimes, ranging from 15 ps to 1.6 ns.^{50–53} In addition, *cis*- $\text{Rh}_2(\text{II,II})$ partial paddlewheel complexes featuring DTolF and F-form bridging ligands also exhibit $^1\text{ML-LCT}$ states with lifetimes of 16 to 100 ps.²² The slower isc rates in bimetallic complexes may be attributable to the rigidity of the paddlewheel architecture. Lower isc rates in

diplatinum paddlewheel and chromium acetylacetonate complexes were previously attributed to a more rigid ligation sphere.^{51,54}

The ground-state IR spectrum of **2** features strong DTolF $\nu(\text{form})$ peaks at 1497 and 1580 cm^{-1} and a weaker band at 1597 cm^{-1} . The $\nu(\text{Ph-form})$ peak appears at 1338 cm^{-1} and additional carboxylate stretches of the npCOO^- ligand are observed at 1426 and 1633 cm^{-1} (Figure 5b). The TRIR spectra of **2** obtained upon 700 nm excitation (IRF \approx 170 fs, 2 μJ) exhibit ground state bleach signals at 1347, 1434, 1503, 1570, and 1627 cm^{-1} (Table S1). Unlike complex **1**, the ground-state features do not recover over the course of the experiment (2.8 ns), such that transient species with $\tau > 5$ ns must be present. This point is most evident in the DTolF $\nu(\text{form})$ bleach signal at 1503 cm^{-1} , which does not shift or change in intensity between 1 ps and 2.8 ns. The positive $\nu(\text{Ph-form})$ signal at 1313 cm^{-1} decays to $\sim 60\%$ of its initial intensity with $\tau \approx 7$ ps, but does not change further throughout the experiment. These features parallel those observed for **1**, leading to the hypothesis that the initially populated $^1\text{ML-LCT}$ state decays with a time constant of ~ 7 ps to populate a long-lived $^3\text{ML-LCT}$ state ($\tau > 5$ ns).

It is evident from the TRIR spectra of **2** shown in Figure 5b that there are changes to the bleach signals at 1570 and 1627 cm^{-1} at early times, but after ~ 20 ps they remain relatively constant and persist up to the longest time point of the experiment, 2.8 ns. The bleach at 1570 cm^{-1} appears to become more negative and shift to lower energies, whereas that at 1627 cm^{-1} appears to decrease in intensity. These observed changes in the negative signals are ascribed to the superposition of a positive $\nu(\text{npCOO}^-)$ feature (Figure S6) positioned between the two ground-state bands, at ~ 1580 cm^{-1} , that shifts to higher energy at later times to ~ 1610 cm^{-1} . The growth of the 1610 cm^{-1} peak takes place with a time constant of 7 ± 2 ps. This band is assigned to a carboxylate stretch of the npCOO^- ligands due to its position, high intensity, and the absence of this peak in **1**. The shift of the carboxylate signal from 1633 cm^{-1} in the ground state to 1590 cm^{-1} upon excitation points at a weakening of the axial Rh–O bond in the $^1\text{ML-LCT}$ excited state, followed by a shift to higher frequencies and regaining some of the axial bond strength as the system intersystem crosses into the $^3\text{ML-LCT}$ state with a time constant of ~ 7 ps. A similar trend is also observed for the excited-state carboxylate signal at 1380 cm^{-1} in the $^1\text{ML-LCT}$ state, which shifts to 1390 cm^{-1} in the $^3\text{ML-LCT}$ state.

The IR spectra observed for complexes **3** and **4** are shown in Figure S3 and parallel those for **1** and **2**, respectively, with $^1\text{ML-LCT}$ and $^3\text{ML-LCT}$ lifetimes listed in Table 1. The most significant difference is the shift in the IR stretches of the DTolF and F-form ligands apparent in the ground and excited states (Figure S7).

Transient Absorption Spectroscopy. The femtosecond transient absorption (fsTA) spectra of **1** in DMSO are shown in Figure 6a ($\lambda_{\text{exc}} = 600$ nm, IRF = 85 fs). At early times, 600 fs, a single broad band is observed that extends from 350 to 550 nm, however, it is apparent that the feature with maximum at ~ 400 nm decays with a concomitant increase in the band at ~ 470 nm, resulting in a signal with maximum at 485 nm at 425 ps. It should be noted that strong absorption is also observed in the 620–660 nm range; however, scattered light from the 600 nm pump pulse obstructed the collection window in the 540–620 nm region. The decrease in intensity at $\lambda > 500$ nm is ascribed to the onset of the strong ground-state absorption with

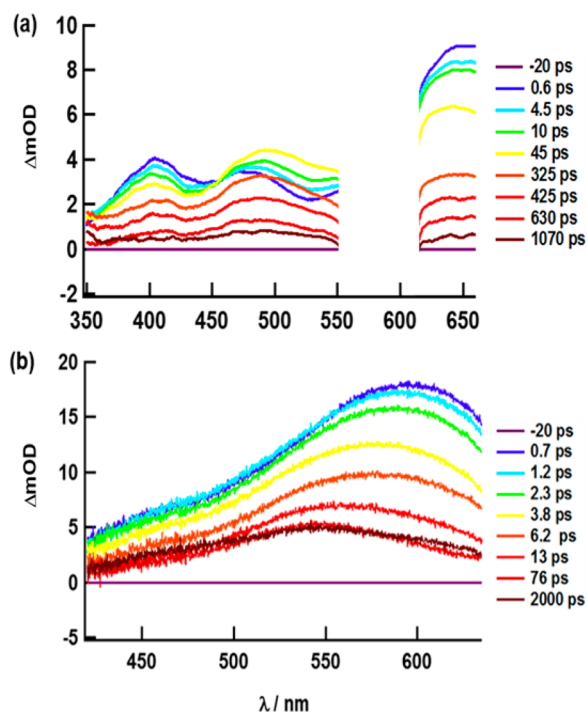


Figure 6. fsTA spectra of (a) **1** ($\lambda_{\text{exc}} = 600$ nm, 2 μJ) and (b) **2** in DMSO ($\lambda_{\text{exc}} = 700$ nm, 2 μJ).

a maximum at 577 nm. The peak at ~ 500 nm increases with a time constant of 11 ps whereas that at 400 nm decreases over 12 ps. The strong absorption at 645 nm can be fitted to a biexponential decay with $\tau_1 = 13$ ps (22%) and $\tau_2 = 445$ ps (78%) (Figure S8).

The observed spectral features are consistent with oxidation of **1** to the corresponding $\text{Rh}_2^{\text{III,II}}$ cation, where the positive charge is localized in the HOMO with DTolF (68%) and Rh_2 (26%) character, and reduction of one of the np ligands (LUMO). The spectroelectrochemistry of **1**, shown in Figure S8, features a broad peak between 340 and 500 nm and strong absorption with maximum at ~ 680 nm upon one-electron oxidation ($E_{\text{app}} = +1.25$ V vs Ag/AgCl). There are relatively small changes upon electrochemical reduction of **1**, but there is a small peak at 350 nm with a shoulder at 445 nm. The broad signal observed in the fsTA spectra is consistent with the positions and superposition of these peaks. These results are in agreement with the assignment from the TRIR data for **1**, where the short and long components were attributed to $^1\text{ML-LCT}$ and $^3\text{ML-LCT}$ excited states, respectively.

The fsTA spectra of **2** upon 700 nm excitation (IRF = 85 fs) reveals similar spectral features to **1**, with a broad peak with maximum at 595 nm at 700 fs (Figure 6b). The superposition of the ground state bleach at 490 nm (Figure 3) gives rise to another apparent peak with maximum at 450 nm. The broad 595 nm band blue-shifts to 545 nm with a lifetime of 7 ps (Figure 6b); no further spectral shifts or signal decay is observed after ~ 20 ps for the duration of the experiment (2.8 ns). Transient absorption spectroscopy of **2** with 532 nm (fwhm ~ 8 ns) excitation reveals that the long-lived state decays with a $\tau \approx 25$ ns, a value that is close to the instrument response function (17 ns).

The broad absorption in the 500–640 nm range is consistent with the superposition of the spectra of the species obtained upon electrochemical reduction ($E_{\text{app}} = -1.40$ V vs Ag/AgCl)

and oxidation ($E_{\text{app}} = +0.950$ V vs Ag/AgCl) of **2** (Figure S8). Based on these results, the TRIR data, and a comparison to **1**, the 7 ps component in **2** is assigned as arising from the ¹ML-LCT excited state which then generates the ³ML-LCT state, and the latter decays with $\tau \approx 25$ ns. The differences in the lifetimes of **1** and **2** are ascribed to the axial coordination of the carboxylate in the latter. The solvent-coordinated axial positions in **1** aid in nonradiative decay pathways, while **2** has a similar excited state without comparable solvent-assisted deactivation pathways available.

Based on the TRIR data, it appears that the ³ML-LCT state of **2** possesses greater metal character than the ¹ML-LCT, evidenced by the strengthening of the rhodium-carboxylate bond. The shifts observed at early times in the fsTA spectrum of **2** as the system intersystem crosses may correspond to greater mixing with higher lying metal-centered MOs, such as $\text{Rh}_2(\text{d}\sigma^*)$, in the triplet manifold than in the lowest energy singlet state. Such mixing would both impart greater Rh_2 character to the MO in which the hole is localized and provide enhanced overlap with the antisymmetric linear combination of the axial oxygen lone pairs, thus strengthening the Rh–O bonds. It has previously been shown in dirhodium formamidinate complexes that the triplet manifold has significant metal centered character.²²

Complexes **3** and **4** exhibit similar transient absorption spectra to those of **1** and **2**, respectively (Figure S9). The ¹ML-LCT and ³ML-LCT lifetimes for **3** were measured to be 9 and 580 ps, whereas those for **4** were 9 ps and 22 ns, respectively.

It should be noted that the charge-transfer character of the lowest energy excited state in complexes **1–4**, which contain a μ^2 -naphthyridine bridging unit, is different than those previously observed for related dirhodium formamidinate complexes of the type $\text{cis-}[\text{Rh}_2(\text{DTolF})_2(\text{L})_2]^{2+}$ ($\text{L} = \text{dpq, dpbz}$). In the latter, the ligand L coordinates in a κ^2 binding mode to each metal. Unlike **1–4**, the lowest energy triplet excited states in these chelated compounds are metal-centered, ³MC, with $\text{Rh}(\text{d}\pi^*)$ -to- $\text{Rh}(\text{d}\sigma^*)$ character.²² The difference in lowest triplet excited state between these two types of systems is attributed to the significantly higher energy of the $\text{Rh}_2(\text{d}\sigma^*)$ orbitals in **1–4**, evidenced by the shorter Rh–Rh crystallographic bond length of 2.4482(4) Å in **2** as compared to those of $\text{cis-}[\text{Rh}_2(\text{F-Form})_2(\text{dpq})_2]^{2+}$ and $\text{cis-}[\text{Rh}_2(\text{DTolF})_2(\text{dpbz})_2]^{2+}$, 2.597(1) Å and 2.5991(9) Å, respectively.

Excited-State Energies and Redox Reactivity. Complexes **1–4** are not emissive at room temperature or 77 K, such that the energy of the ³ML-LCT, E_{00}^{T} , of the complexes cannot be readily obtained from the luminescence. Instead, a series of organic molecules with varying ³ $\pi\pi^*$ energies were utilized to estimate E_{00}^{T} of **1–4**. In these experiments, the organic sensitizers were used as energy-transfer donors (EnDs) from their long-lived ³ $\pi\pi^*$ excited states. The monoexponential decay of the transient absorption signal from each EnD was monitored as a function of Rh_2 complex concentration, permitting the generation of Stern–Volmer plots, τ_0/τ vs $[\text{Rh}_2]$, for each EnD/ Rh_2 pair and calculation of the energy-transfer quenching rate constant, k_{En}^{T} , from the slope of each plot.

As an example, Figure S11 shows the kinetic traces for decay of the ³ $\pi\pi^*$ state of anthracene, with energy $E^{\text{T}} = 1.83$ eV,³⁵ as the EnD as a function of increasing concentrations of **1**. The lifetime of the ³ $\pi\pi^*$ of anthracene decreases from $\tau_0 = 44.4$ μs with the addition of **1**, resulting in a triplet–triplet energy-transfer rate constant, k_{En}^{T} , of 2.15×10^9 $\text{M}^{-1} \text{s}^{-1}$. The values of

k_{En}^{T} measured for all EnD/ Rh_2 complex pairs are listed in Table S1. Oxidative and reductive quenching of the ³ $\pi\pi^*$ states have been ruled out based on the lack of charge-transfer products in the transient absorption spectra. Moreover, for all the EnD/ Rh_2 complex pairs, charge transfer from the EnD ³ $\pi\pi^*$ state to **1–4** is calculated to be thermodynamically unfavorable. In addition, the quenching rate constants do not follow a trend of ease of reduction/oxidation of the quenchers, as would be expected for oxidative/reductive quenching.

The values of k_{En}^{T} decrease with the ³ $\pi\pi^*$ energy of the EnD, E^{T} . Complexes **1–4** quench the ³ $\pi\pi^*$ states of sensitizers with $E^{\text{T}} \geq 1.15$ eV, but do not affect the lifetime of β -carotene, with $E^{\text{T}} = 0.78$ eV (Table S1).³⁵ There is a large decrease in the energy-transfer rate constants of rubrene ($E^{\text{T}} = 1.15$ eV, $k_{\text{En}}^{\text{T}} \approx 10^8$ $\text{M}^{-1} \text{s}^{-1}$) by **1–4** relative to those measured for perylene ($E^{\text{T}} = 1.53$ eV, $k_{\text{En}}^{\text{T}} \approx 10^9$ $\text{M}^{-1} \text{s}^{-1}$). These results lead to the estimation that the ³ML-LCT states of **1–4** lie ~ 1.1 eV above the ground state.

The injection of electrons and holes into semiconductors is known to primarily take place from singlet states, including in Ru(II) complexes with sub-picosecond ¹MLCT lifetimes.^{6,55} Therefore, it is also important to estimate the ¹ML-LCT energies of **1–4**, E_{00}^{S} , especially given the picosecond singlet lifetimes of these Rh_2 complexes. A value of $E_{00}^{\text{S}} \approx 1.7$ eV was estimated by the absorption spectrum of **2** at 77 K in an EtOH:MeOH (5:1) glass, which shows little vibronic progression in the lowest ¹ML-LCT transition but does have a large absorption onset at ~ 710 nm (~ 1.7 eV; Figure S13). Using this method, E_{00}^{S} energies of 2.0, 2.1, and 1.8 eV were estimated from the 77 K absorption for **1**, **3**, and **4** (Table S3).

The values of E_{00}^{S} and E_{00}^{T} , together with the measured oxidation and reduction potentials (Table 1), were used to estimate the singlet and triplet excited-state oxidation and reduction potentials (¹ E_{ox}^* /³ E_{ox}^* and ¹ E_{red}^* /³ E_{red}^*) of **1–4**, respectively (Table S3). The Latimer diagram in Figure 7 was

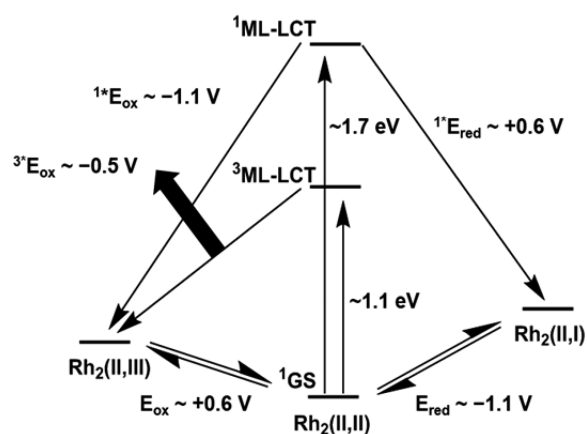


Figure 7. Latimer diagram showing the ground- and excited-state reduction potentials of **2** vs Ag/AgCl.

derived for **2**, using $E_{\text{red}} = -1.1$ vs Ag/AgCl and $E_{\text{ox}} = +0.6$ vs Ag/AgCl and the calculated values of ¹ E_{ox}^* and ³ E_{red}^* for the singlet and triplet states with $E_{00}^{\text{S}} \approx 1.7$ eV and $E_{00}^{\text{T}} \approx 1.1$ eV. Based on the values of ¹ $E_{\text{ox}}^* \approx -1.1$ V and ³ $E_{\text{ox}}^* \approx -0.5$ V vs Ag/AgCl (Figure 7), both the ¹ML-LCT and ³ML-LCT excited state are expected to possess sufficient energy for the reduction of n-type semiconductors, such as anatase TiO_2 ($E_{\text{CB}} = -0.4$ V vs Ag/AgCl).⁵⁶ Similarly, with ¹ $E_{\text{red}}^* \approx +0.6$ V, complex **2** should be able to oxidize p-type semiconductors, such as NiO

($E_{\text{VB}} = +0.2\text{--}0.3$ V vs Ag/AgCl).⁵⁷ These values are similar to comparable sensitizers. Commonly used dyes for TiO₂ sensitization such as squareine and N3 dye have singlet excited-state oxidation potentials of -1.1 and -1.3 V vs Ag/AgCl,^{14,58} respectively, while commonly used p-type dyes on NiO have singlet excited-state reduction potentials spanning $+0.8$ to $+1.4$ V vs Ag/AgCl,⁵⁹ which are more favorable than complex **2** ($+0.6$ V vs Ag/AgCl), but similar to complexes **1** and **3** ($+1.1$ and $+1.2$ V vs Ag/AgCl, respectively).

In order to show that these Rh₂(II,II) complexes are redox active upon irradiation, the ability of **2** to undergo bimolecular excited-state electron transfer to MV²⁺ was probed. The ³ML-LCT excited state of **2** is sufficiently long-lived, $\tau \approx 25$ ns, with ${}^3E_{\text{ox}} = -0.5$ V vs Ag/AgCl, has a favorable driving force to form reduced MV²⁺, where $E_{1/2}(\text{MV}^{2+/+}) \approx -0.40$ V vs Ag/AgCl in polar organic solvents.⁶⁰ The excitation of **2** ($300 \mu\text{M}$) with 532 nm light (fwhm ~ 8 ns) in the presence of MV²⁺ (30 mM) in either DMSO or H₂O:CH₃CN mixtures resulted in the observation of the well-known spectral features of the one-electron reduced MV⁺ radical at 395 and 605 nm, which persisted on the order of microseconds (Figure S12).⁶¹ In order to gauge the usefulness of **2** in a multicomponent system, the sacrificial electron donor BNAH (0.7 M) was added to a solution of MV²⁺ (50 mM) and **2** ($300 \mu\text{M}$). Steady-state photolysis ($\lambda_{\text{irr}} > 610$ nm) over the course of 5 min resulted in the formation of the blue color and electronic absorption spectrum associated with MV⁺ radical (Figure S14). In this multicomponent system, MV²⁺ is reduced by the ³ML-LCT excited state of **2**, followed by reduction of the oxidized complex by BNAH. This mechanism is consistent with the observation of the MV²⁺ reduction observed in the transient absorption experiments in the absence of BNAH and the unfavorable driving force calculated for the excited-state reduction of **2** (${}^3E_{\text{red}} \approx 0.0$ V) by BNAH ($E_{1/2}(\text{BNAH}^{+/0}) = +0.615$ V in CH₃CN vs Ag/AgCl).

CONCLUSIONS

A series of dirhodium paddlewheel complexes, **1–4**, that absorb from the ultraviolet to the near-IR were synthesized and their redox and photophysical properties were characterized. The ¹ML-LCT and relatively long ³ML-LCT excited states of the complexes were investigated using transient absorption and time-resolved IR spectroscopies. Complexes **2** and **4** have E_{00}^{T} and E_{00}^{S} values of ~ 1.1 and ~ 1.7 eV, respectively. The ³ML-LCT of **2** undergoes electron-transfer reactions upon excitation with low energy light. In general, these represent a new class of complexes with panchromatic absorption that extends well beyond the absorption spectra of typical Ru(II) dyes used in solar cells. The excited-state redox reactivity shown for these complexes, coupled with the extended absorption profile, makes them a potential new class of dyes for solar energy conversion applications, including dye-sensitized solar cells and light absorbers in photocatalysis for the production of fuels from abundant sources.

ASSOCIATED CONTENT

Supporting Information

The Supporting Information is available free of charge on the ACS Publications website at DOI: 10.1021/jacs.7b08489.

Detailed instrumentation and methods, synthetic schemes, electronic absorption spectra, cyclic voltammograms, ATR-IR spectra, fsTA and TRIR kinetic traces, 77

K absorption spectra, ES redox potentials, quenching constants calculations, and crystallographic coordinates, including Figures S1–S14 and Tables S1–S3 (PDF)
X-ray crystallographic data for **2** (CIF)

AUTHOR INFORMATION

Corresponding Author

*turro.1@osu.edu

ORCID

Travis A. White: 0000-0002-6200-4416

Claudia Turro: 0000-0003-3202-5870

Present Address

[†]T.A.W.: Department of Chemistry and Biochemistry, Ohio University, Athens, OH 45701, USA.

Notes

The authors declare no competing financial interest.

ACKNOWLEDGMENTS

C.T. thanks the U.S. Department of Energy, Office of Science, Office of Basic Energy Sciences (DE-SC0010542), for their financial support of this research. The authors further thank the Center for Chemical and Biophysical Dynamics at Ohio State for collection of all infrared data and femtosecond transient absorption and the Ohio State Supercomputer Center⁶² for computational resources. We also thank the lab of Prof. Abraham Badu-Tawiah for use of a microbalance.

REFERENCES

- (1) Key World Energy Statistics, 2016; <http://www.iea.org/publications/freepublications/publication/KeyWorld2016.pdf> (accessed Apr 30, 2017).
- (2) Tsao, J.; Lewis, N.; Crabtree, G. Solar FAQs, 2006.
- (3) Kahle, A. B.; Weill, G.; Carter, W. D.; Ulaby, F. T.; Siqueira, P.; Nashashibi, A.; Sarabandi, K. *Proc. IEEE* **2003**, *63*, 137.
- (4) Moan, J.; Juzeniene, A. *J. Photochem. Photobiol., B* **2010**, *101*, 109.
- (5) Brennaman, M. K.; Dillon, R. J.; Alibabaei, L.; Gish, M. K.; Dares, C. J.; Ashford, D. L.; House, R. L.; Meyer, G. J.; Papanikolas, J. M.; Meyer, T. J. *J. Am. Chem. Soc.* **2016**, *138*, 13085.
- (6) Hagfeldt, A.; Boschloo, G.; Sun, L.; Kloo, L.; Pettersson, H. *Chem. Rev.* **2010**, *110*, 6595.
- (7) Robertson, N. *Angew. Chem., Int. Ed.* **2006**, *45*, 2338.
- (8) Pashaei, B.; Shahroosvand, H.; Graetzel, M.; Nazeeruddin, M. K. *Chem. Rev.* **2016**, *116*, 9485.
- (9) Reece, S. Y.; Hamel, J. A.; Sung, K.; Jarvi, T. D.; Esswein, A. J.; Pijpers, J. J. H.; Nocera, D. G. *Science* **2011**, *334*, 645.
- (10) Hammarström, L. *Acc. Chem. Res.* **2015**, *48*, 840.
- (11) Campagna, S.; Puntoriero, F.; Nastasi, F.; Bergamini, G.; Balzani, V. In *Photochemistry and Photophysics of Coordination Compounds I*; Balzani, V., Campagna, S., Eds.; Springer: Berlin/Heidelberg, 2007; Vol. 280, pp 117–214.
- (12) Nazeeruddin, M. K.; Kay, A.; Rodicio, I.; Humphry-Baker, R.; Mueller, E.; Liska, P.; Vlachopoulos, N.; Graetzel, M. *J. Am. Chem. Soc.* **1993**, *115*, 6382.
- (13) Joseph, K. L. V.; Lim, J.; Anthonysamy, A.; Kim, H.; Choi, W.; Kim, J. K. *J. Mater. Chem. A* **2015**, *3*, 232–239.
- (14) Rao, G. H.; Venkateswararao, A.; Giribabu, L.; Han, L.; Bedja, I.; Gupta, R. K.; Islam, A.; Singh, S. P. *Phys. Chem. Chem. Phys.* **2016**, *18*, 14279.
- (15) Li, L.-L.; Diau, E. W.-G. *Chem. Soc. Rev.* **2013**, *42*, 291.
- (16) Wang, C.-L.; Hu, J.-Y.; Wu, C.-H.; Kuo, H.-H.; Chang, Y.-C.; Lan, Z.-J.; Wu, H.-P.; Wei-Guang Diau, E.; Lin, C.-Y. *Energy Environ. Sci.* **2014**, *7*, 1392.
- (17) Xie, Y.; Tang, Y.; Wu, W.; Wang, Y.; Liu, J.; Li, X.; Tian, H.; Zhu, W.-H. *J. Am. Chem. Soc.* **2015**, *137*, 14055.

- (18) Ince, M.; Yum, J.-H.; Kim, Y.; Mathew, S.; Grätzel, M.; Torres, T.; Nazeeruddin, M. K. *J. Phys. Chem. C* **2014**, *118*, 17166.
- (19) Qin, P.; Zhu, H.; Edvinsson, T.; Boschloo, G.; Hagfeldt, A.; Sun, L. *J. Am. Chem. Soc.* **2008**, *130*, 8570.
- (20) Ji, Z.; Natu, G.; Wu, Y. *ACS Appl. Mater. Interfaces* **2013**, *5*, 8641.
- (21) Chisholm, M. H.; Gustafson, T. L.; Turro, C. *Acc. Chem. Res.* **2013**, *46*, 529–538.
- (22) Li, Z.; Leed, N. A.; Dickson-Karn, N. M.; Dunbar, K. R.; Turro, C. *Chem. Sci.* **2014**, *5*, 727–737.
- (23) Brown-Xu, S. E.; Chisholm, M. H.; Durr, C. B.; Gustafson, T. L.; Spilker, T. F. *J. Am. Chem. Soc.* **2014**, *136*, 11428–11435.
- (24) White, T. A.; Dunbar, K. R.; Thummel, R. P.; Turro, C. *Polyhedron* **2016**, *103*, 172.
- (25) Catalan, K. V.; Mindiola, D. J.; Ward, D. L.; Dunbar, K. R. *Inorg. Chem.* **1997**, *36*, 2458.
- (26) Fulmer, G. R.; Miller, A. J. M.; Sherden, N. H.; Gottlieb, H. E.; Nudelman, A.; Stoltz, B. M.; Bercaw, J. E.; Goldberg, K. I. *Organometallics* **2010**, *29*, 2176.
- (27) SAINT; Bruker Analytical X-Ray Instruments, Inc.: Madison, WI.
- (28) APEX2; Bruker Analytical X-Ray Instruments, Inc.: Madison, WI.
- (29) Sheldrick, G. SADABS; University of Gottingen, Germany.
- (30) Sheldrick, G. M. *Acta Crystallogr., Sect. A: Found. Adv.* **2015**, *71*, 3.
- (31) *International Tables for Crystallography*; Kluwer Academic Publishers: Dordrecht, 1992; Vol. C.
- (32) Bradley, P. M.; Bursten, B. E.; Turro, C. *Inorg. Chem.* **2001**, *40*, 1376.
- (33) Burdzinski, G.; Hackett, J. C.; Wang, J.; Gustafson, T. L.; Hadad, C. M.; Platz, M. S. *J. Am. Chem. Soc.* **2006**, *128*, 13402.
- (34) Wang, J.; Burdzinski, G.; Kubicki, J.; Gustafson, T. L.; Platz, M. S. *J. Am. Chem. Soc.* **2008**, *130*, 5418.
- (35) Murov, S. L. *Handbook of Photochemistry XI*; Marcel Dekker, Inc.: New York, 1973. *J. Prakt. Chem.* **1976**, *318*, 702–703.
- (36) Frisch, M. J.; Trucks, G. W.; B, S. H.; Scuseria, G. E.; Robb, M. A.; Cheeseman, J. R.; Scalmani, G.; Barone, V.; Mennucci, B.; Petersson, G. A.; et al. *Gaussian 09*; Gaussian, Inc., 2013.
- (37) Andrae, D.; Haußermann, U.; Dolg, M.; Stoll, H.; Preuß, H. *Theor. Chim. Acta* **1990**, *77*, 123–141.
- (38) Dennington, R.; Keith, T.; Millan, J. *Gaussview*; Semichem Inc.: Shawnee Mission, KS, 2007.
- (39) Gorelsky, S. I.; Lever, A. B. P. *J. Organomet. Chem.* **2001**, *635*, 187.
- (40) Kauffman, G. B. *Angew. Chem., Int. Ed.* **2007**, *46*, 2565.
- (41) Tresoldi, G.; Lo Schiavo, S.; Nicolò, F.; Cardiano, P.; Piraino, P. *Inorg. Chim. Acta* **2003**, *344*, 190.
- (42) Paudler, W. W.; Kress, T. J. In *Advances in Heterocyclic Chemistry*; Elsevier: Amsterdam, 1970; Vol. 11, pp 123–175.
- (43) Bursten, B. E.; Cotton, F. A. *Inorg. Chem.* **1981**, *20*, 3042.
- (44) Sowa, T.; Kawamura, T.; Shida, T.; Yonezawa, T. *Inorg. Chem.* **1983**, *22*, 56.
- (45) Dubicki, L.; Martin, R. L. *Inorg. Chem.* **1970**, *9*, 673.
- (46) Fillman, K. L.; Przyojski, J. A.; Al-Afyouni, M. H.; Tonzetich, Z. J.; Neidig, M. L. *Chem. Sci.* **2015**, *6*, 1178–1188.
- (47) Bridgeman, A. J.; Cavigliasso, G.; Ireland, L. R.; Rothery, J. J. *Chem. Soc., Dalton Trans.* **2001**, *14*, 2095.
- (48) Bhasikuttan, A. C.; Suzuki, M.; Nakashima, S.; Okada, T. *J. Am. Chem. Soc.* **2002**, *124*, 8398.
- (49) Forster, L. S. *Coord. Chem. Rev.* **2006**, *250*, 2023.
- (50) Fox, L. S.; Marshall, J. L.; Gray, H. B.; Winkler, J. R. *J. Am. Chem. Soc.* **1987**, *109*, 6901.
- (51) Durrell, A. C.; Keller, G. E.; Lam, Y.-C.; Sýkora, J.; Vlček, A.; Gray, H. B. *J. Am. Chem. Soc.* **2012**, *134*, 14201–14207.
- (52) Miskowski, V. M.; Rice, S. F.; Gray, H. B.; Milder, S. J. *J. Phys. Chem.* **1993**, *97*, 4277–4283.
- (53) Alberding, B. G.; Chisholm, M. H.; Gustafson, T. L. *Inorg. Chem.* **2012**, *51*, 491.
- (54) Schrauben, J. N.; Dillman, K. L.; Beck, W. F.; McCusker, J. K. *Chem. Sci.* **2010**, *1*, 405.
- (55) Black, F. A.; Clark, C. A.; Summers, G. H.; Clark, I. P.; Towrie, M.; Penfold, T.; George, M. W.; Gibson, E. A. *Phys. Chem. Chem. Phys.* **2017**, *19*, 7877.
- (56) Xu, Y.; Schoonen, M. A. A. *Am. Mineral.* **2000**, *85*, 543.
- (57) Buchalska, M.; Kuncewicz, J.; Świętek, E.; Łabuz, P.; Baran, T.; Stochel, G.; Macyk, W. *Coord. Chem. Rev.* **2013**, *257*, 767.
- (58) Furube, A.; Katoh, R.; Hara, K. *Surf. Sci. Rep.* **2014**, *69*, 389.
- (59) Odobel, F.; Le Pleux, L.; Pellegrin, Y.; Blart, E. *Acc. Chem. Res.* **2010**, *43*, 1063.
- (60) Bird, C. L.; Kuhn, A. T. *Chem. Soc. Rev.* **1981**, *10*, 49.
- (61) Peon, J.; Tan, X.; Hoerner, J. D.; Xia, C.; Luk, Y. F.; Kohler, B. J. *Phys. Chem. A* **2001**, *105*, 5768.
- (62) Ohio Supercomputer Center, Columbus, OH, 1987; <http://osc.edu/ark:/19495/f5s1ph73>.